

The 27th Annual Workshop on Mathematical  
Problems in Industry:  
Matched Asymptotic Solutions of Glass  
Temperature Profiles During Optical Fibre  
Drawing

Report prepared by:

C. J. W. Breward, I. M. Griffiths, H. Potter & M. Taroni

Participants:

R. Beckham<sup>1</sup>, C. J. W. Breward<sup>2</sup>, L. J. Cummings<sup>3</sup>,  
A. Fillipov<sup>4</sup>, M. Gratton<sup>5</sup>, I. M. Griffiths<sup>2</sup>, M. Kanoria<sup>6</sup>,  
K. Kilgore<sup>7</sup>, V. Lapin<sup>8</sup>, T-S. Lin<sup>3</sup>, M. Ma<sup>3</sup>, H. Nganguia<sup>3</sup>,  
J. Pohlmeier<sup>3</sup>, H. Potter<sup>9</sup>, D. Schwendeman<sup>10</sup>, P. Tandon<sup>4</sup>,  
M. Taroni<sup>2</sup>, & H. Yaple<sup>5</sup>.

<sup>1</sup> University of Texas at Tyler, <sup>2</sup> University of Oxford, <sup>3</sup> NJIT,

<sup>4</sup> Corning Inc., <sup>5</sup> Northwestern University, <sup>6</sup> University of Calcutta,

<sup>7</sup> Drexel University, <sup>8</sup> University of Limerick, <sup>9</sup> Duke University,

<sup>10</sup> Rensselaer Polytechnic Institute.

February 6, 2012

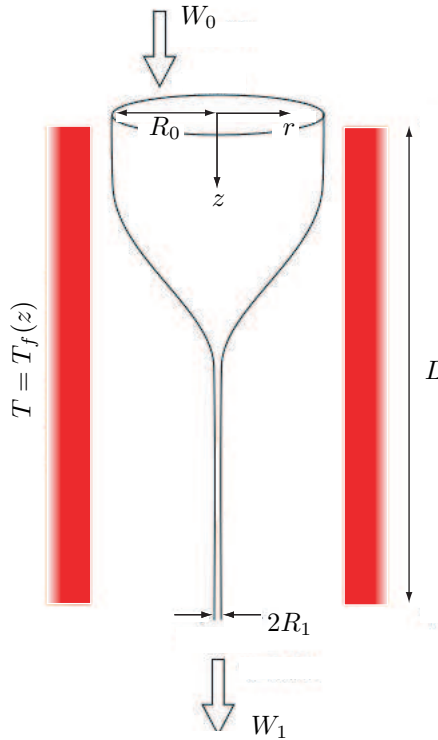


Figure 1: Schematic diagram for the construction of glass fibres via the downdraw method.

## 1 Introduction

Corning Incorporated, the world leader in specialty glass and ceramics, is the largest manufacturer of fibre-optic cables for the telecommunications industry. Early stages of the manufacturing process create what is known as a preform, which is a cylindrical rod with a diameter of around 5 centimetres comprising a thin cylindrical core, of diameter about 8 microns, of glass containing dopants, surrounded by an annulus of exceptionally pure glass. The dopants raise the refractive index of the core so that light waves that hit the internal boundary at a glancing angle undergo total internal reflection. It is this phenomenon that allows light waves to propagate through the fibre. In order to make a product of practical use this preform must be drawn into a

thin fibre in which the outer region, known as the cladding, has a diameter of around 125 microns. The glass is drawn, under tension, through a furnace, in which the preform melts, its viscosity decreases, and the change in thickness is achieved. As it exits the furnace, the glass is cooled by the air and solidifies into the desired solid glass fibre. A schematic of the process is shown in figure 1.

Corning would like to understand more clearly the thermodynamics of this drawing process and, in particular, explain why there is such a sharp change in the fibre thickness as the temperature is varied. Of particular interest to Corning is the effect of the radiation on the temperature of the glass, and its relative importance to convective heat transfer. Furthermore, given that solving a full three-dimensional radiative heat transfer problem is very numerically intensive (see, for example, Choudhury et al., 1999), Corning are interested in seeking simplified models that can quickly give useful insight into the parameter dependencies and hence aid their understanding of the process.

With this in mind, the starting point for our analysis is the work of Huang et al. (2008), who investigated dopant diffusion within the fibre drawing process, deriving asymptotic solutions for the temperature and fibre radius profiles. However, their model does not include radiative heat transfer, incorporating instead a sharp cut-off between a heating and a cooling region that were both assumed to be due to convection alone. It is therefore our aim to improve on this model by eliminating this artificial cut-off and instead include both radiative and convective heat transfer throughout the process and determine where each mechanism dominates. Once our model is derived, we exploit both the large aspect ratio of the fibre and the relative orders of magnitude of the parameters to reduce the problem to a one- or two-dimensional system of equations that may be readily solved numerically and for which some approximate analytical solutions exist. We are able to predict many of the qualitative features observed by Corning, such as the sharp transition in fibre thickness, validating our approach and suggesting that our model may be used for quick scenario testing and for comparison to the full three-dimensional simulations performed by Corning.

Parameter	Symbol	Approximate value	Units
density	$\rho$	2500	$\text{kg m}^{-3}$
viscosity	$\hat{\mu}$	$10^3\text{--}10^8$	$\text{N s m}^{-2}$
tubing length	$L$	0.5	m
initial radius	$R_0$	5	cm
heat transfer coefficient	$k_h$	100	$\text{W m}^{-2}$
input speed	$W_0$	$10^{-3}$	$\text{m s}^{-1}$
draw speed	$W_1$	30	$\text{m s}^{-1}$
maximum furnace temperature	$T^*$	2500	K
specific heat	$c_p$	1200	$\text{J kg}^{-1} \text{K}^{-1}$
thermal conductivity	$k_c$	1.1	$\text{W m}^{-1} \text{K}^{-1}$
Stefan–Boltzmann constant	$\sigma$	$5.67 \times 10^{-8}$	$\text{W m}^{-2} \text{K}^{-4}$
specific emissivity	$\varepsilon_r$	1	—
input viscosity	$\hat{\mu}_0$	$2 \times 10^3$	Pas
refractive index	$n_0$	1.5	—
absorption coefficient <sup>1</sup>	$\chi$	$2 \times 10^2$	$\text{m}^{-1}$

Table 1: Typical parameter values for the drawing of glass tubing (Huang et al., 2003; Šarboh et al., 1998; National Institute of Standards & Technology, 1991; Paek and Runk, 1978).

## 2 Problem Description

During the manufacture of optical fibres, it is necessary to heat the glass preform until its viscosity has decreased to the point where the glass, which is an amorphous solid at room temperature, behaves as a liquid and can be drawn out into a thin fibre. We seek to describe the steady-state behaviour of the liquid glass during this drawing process, that is, the shape, velocity profile, and temperature profile of the glass in the steady-state manufacturing process. We ignore any affect of dopants on the material properties of the glass.

### 2.1 Governing equations

We consider the steady-state configuration where the input radius of the fibre preform is  $R_0$  and the length of the furnace is  $L$ , as depicted in figure 1. Based on typical parameter values for the process, given in table 1, we find

that the Reynolds number for the flow is very small and so the fluid flow is governed by the slow-flow equations (Fitt et al., 2002),

$$\frac{1}{\hat{r}} \frac{\partial}{\partial \hat{r}} (\hat{r} \hat{u}) + \frac{\partial \hat{w}}{\partial \hat{z}} = 0, \quad (1a)$$

$$-\frac{\partial \hat{p}}{\partial \hat{r}} + \frac{\partial}{\partial \hat{z}} \left( \hat{\mu} \frac{\partial \hat{u}}{\partial \hat{z}} \right) + \hat{\mu} \frac{\partial}{\partial \hat{r}} \left( \frac{1}{\hat{r}} \frac{\partial}{\partial \hat{r}} \left( \hat{r} \frac{\partial \hat{u}}{\partial \hat{r}} \right) \right) + \frac{\partial \hat{\mu}}{\partial \hat{z}} \frac{\partial \hat{w}}{\partial \hat{r}} + 2 \frac{\partial \hat{\mu}}{\partial \hat{r}} \frac{\partial \hat{u}}{\partial \hat{r}} = 0, \quad (1b)$$

$$-\frac{\partial \hat{p}}{\partial \hat{z}} + \frac{\partial}{\partial \hat{z}} \left( 2 \hat{\mu} \frac{\partial \hat{w}}{\partial \hat{z}} \right) + \frac{1}{\hat{r}} \frac{\partial}{\partial \hat{r}} \left( \hat{\mu} \hat{r} \frac{\partial \hat{w}}{\partial \hat{r}} \right) + \frac{1}{\hat{r}} \frac{\partial}{\partial \hat{r}} \left( \hat{\mu} \hat{r} \frac{\partial \hat{u}}{\partial \hat{z}} \right) = 0, \quad (1c)$$

where  $\hat{r}$  and  $\hat{z}$  denote the radial and axial coordinates,  $\hat{p}$  is the pressure within the molten glass,  $\hat{u}$  and  $\hat{w}$  are the radial and axial velocities of the glass, and  $\hat{\mu}$  is its viscosity, which may in general vary across both along and across the fibre. At the centre of the fibre, symmetry provides the conditions

$$\hat{u} = \frac{\partial \hat{w}}{\partial \hat{r}} = 0, \quad (2a)$$

on  $\hat{r} = 0$ , while the kinematic and dynamic boundary conditions are

$$\hat{u} = \hat{w} \frac{d\hat{R}}{d\hat{z}}, \quad (2b)$$

$$\left( -\hat{p} + 2\hat{\mu} \frac{\partial \hat{u}}{\partial \hat{r}} \right) = \hat{\mu} \frac{d\hat{R}}{d\hat{z}} \left( \frac{\partial \hat{u}}{\partial \hat{z}} + \frac{\partial \hat{w}}{\partial \hat{r}} \right), \quad (2c)$$

$$\hat{\mu} \left( \frac{\partial \hat{u}}{\partial \hat{z}} + \frac{\partial \hat{w}}{\partial \hat{r}} \right) = \frac{d\hat{R}}{d\hat{z}} \left( -\hat{p} + 2\hat{\mu} \frac{\partial \hat{w}}{\partial \hat{z}} \right), \quad (2d)$$

on the glass–air interface  $\hat{r} = \hat{R}(\hat{z})$ , where we are neglecting any effects due to surface tension. The fluid problem is closed by specifying the velocity at the two ends of the tubing,

$$\hat{w}(\hat{r}, \hat{z} = 0) = W_0, \quad \hat{w}(\hat{r}, \hat{z} = L) = W_1, \quad (2e)$$

although we note that, in practice, it is also possible to specify the tension at  $z = L$  rather than the speed.

The viscosity of glass varies significantly with temperature. For the types of glass used by Corning this is well characterized by (Myers, 1989)

$$\hat{\mu} = \hat{\mu}(T_{ref}) \exp \left( \frac{b_1}{\hat{T}} - a_1 \right) \quad (3)$$

where  $T_{ref}$  is a reference temperature and  $a_1, b_1$  are empirically determined constants.

The equation governing the distribution of temperature is

$$\rho c_p \left( \hat{u} \frac{\partial \hat{T}}{\partial \hat{r}} + w \frac{\partial \hat{T}}{\partial \hat{z}} \right) = \frac{1}{\hat{r}} \frac{\partial}{\partial \hat{r}} \left( k(T) \hat{r} \frac{\partial \hat{T}}{\partial \hat{r}} \right) + \frac{\partial}{\partial \hat{z}} \left( k(T) \frac{\partial \hat{T}}{\partial \hat{z}} \right), \quad (4)$$

where the left-hand side represents thermal convection and the right-hand side thermal conduction, with  $k(T)$  denoting the conductivity of glass. For transparent materials, radiative transfer within the material is of significance, especially at high temperatures. As a result, a radiation contribution must be added to the conventional thermal conductivity,  $k_c$ , so that the apparent conductivity  $k(T) = k_c + k_r(T)$ , where (Paek and Runk, 1978)

$$k_r(T) = \frac{16n_0^2\sigma\hat{T}^3}{3\chi}. \quad (5)$$

Here  $\sigma$  is the Stefan–Boltzmann constant and  $n_0$  and  $\chi$  denote the refractive index and absorption coefficient for the glass (with typical values given in table 1).

The boundary condition at the glass–air interface  $\hat{r} = \hat{R}(\hat{z})$  is

$$-k \frac{\partial \hat{T}}{\partial \hat{r}} = \sigma \varepsilon_R \left( \hat{T}^4 - \hat{T}_f^4 \right) + k_h \left( \hat{T} - \hat{T}_a \right). \quad (6)$$

Here  $\varepsilon_R$  is the specific emissivity and  $k_h$  is the heat transfer coefficient (with typical values given in table 1);  $\hat{T}_f = \hat{T}_f(\hat{z})$  and  $\hat{T}_a = \hat{T}_a(\hat{z})$  are the furnace and ambient air temperatures, both of which are assumed to be known. (In practice, the air temperature would need to be determined as part of the solution.) The terms on the right-hand side represent respectively radiative transfer and convective heating to the surroundings via Newton cooling (Carslaw and Jaeger, 1959). Finally, the system is closed by specifying the input temperature  $\hat{T} = \hat{T}_0$  at  $\hat{z} = 0$ . Here we assume that  $\hat{T}_0$  is a constant, so that  $\partial \hat{T}_0 / \partial \hat{r} = 0$  and, assuming continuity in the temperature, (6) implies that  $\hat{T}_0$  is given by the solution to the quartic equation

$$\sigma \varepsilon_R \left( \hat{T}_0^4 - \hat{T}_f(0)^4 \right) + k_h \left( \hat{T}_0 - \hat{T}_a(0) \right) = 0. \quad (7)$$

However we note that, in practice, if the value of  $\hat{T}_0$  is not given by (7) then there will be a small transient near the inlet over which the system quickly adjusts to this value.

We note that the respective conductive components in (4) may be separated to give

$$\begin{aligned} \rho c_p \left( \hat{u} \frac{\partial \hat{T}}{\partial \hat{r}} + w \frac{\partial \hat{T}}{\partial \hat{z}} \right) &= \frac{1}{\hat{r}} \frac{\partial}{\partial \hat{r}} \left( k_c \hat{r} \frac{\partial \hat{T}}{\partial \hat{r}} \right) + \frac{\partial}{\partial \hat{z}} \left( k_c \frac{\partial \hat{T}}{\partial \hat{z}} \right) \\ &+ \frac{1}{\hat{r}} \frac{\partial}{\partial \hat{r}} \left( \tilde{k}_r \hat{r} \frac{\partial \hat{T}^4}{\partial \hat{r}} \right) + \frac{\partial}{\partial \hat{z}} \left( \tilde{k}_r \frac{\partial \hat{T}^4}{\partial \hat{z}} \right), \end{aligned} \quad (8)$$

where  $\tilde{k}_r = k_r/4\hat{T}^3$ . This equation corresponds to making the assumption that the fibre is optically thick, that is, much thicker than the absorption length-scale. The assumption may break down once the fibre is drawn down to a thickness of  $O(100 \mu\text{m})$ , at which point one might expect the glass to absorb the radiation directly from the surrounding furnace and re-radiate heat back to the furnace. Nevertheless, given that the absorption lengthscale is highly dependent on the glass properties and radiation wavelength, in the interest of simplicity we limit ourselves to considering only the optically thick limit.†

### 3 Non-dimensionalization

We exploit the slenderness of the geometry, that is, we introduce the inverse aspect ratio  $\epsilon = R_0/L \approx 0.1 \ll 1$ , and scale via

$$\begin{aligned} \hat{r} &= \epsilon L r, & \hat{z} &= L z, & \hat{u} &= \epsilon W_0 u, & \hat{w} &= W_0 w, \\ \hat{R} &= \epsilon R, & \hat{T} &= \hat{T}^* T, & \hat{p} &= \frac{\hat{\mu}_0 W_0}{\epsilon^2 L} p, & \hat{\mu} &= \hat{\mu}_0 \mu, \end{aligned} \quad (9)$$

where  $W_0$  is the input axial velocity,  $T^*$  the maximum furnace temperature, and  $\hat{\mu}_0$  the viscosity at  $T^*$ .

---

†We note that one can tackle the optically thin limit in an *ad hoc* manner by including an additional radiative term in the temperature equation (4), as done in Fitt et al. (2002).

Substituting into (1) and (4) provides the dimensionless equations

$$\frac{1}{r} \frac{\partial}{\partial r} (ru) + \frac{\partial w}{\partial z} = 0, \quad (10a)$$

$$-\frac{\partial p}{\partial r} + \epsilon^4 \frac{\partial}{\partial z} \left( \mu \frac{\partial u}{\partial z} \right) + \epsilon^2 \mu \frac{\partial}{\partial r} \left( \frac{1}{r} \frac{\partial}{\partial r} (ru) \right) + \epsilon^2 \frac{\partial \mu}{\partial z} \frac{\partial w}{\partial r} + 2\epsilon^2 \frac{\partial \mu}{\partial r} \frac{\partial u}{\partial r} = 0, \quad (10b)$$

$$-\frac{\partial p}{\partial z} + \epsilon^2 \frac{\partial}{\partial z} \left( 2\mu \frac{\partial w}{\partial z} \right) + \frac{1}{r} \frac{\partial}{\partial r} \left( \mu r \frac{\partial w}{\partial r} \right) + \frac{\epsilon^2}{r} \frac{\partial}{\partial r} \left( \mu r \frac{\partial u}{\partial z} \right) = 0, \quad (10c)$$

$$\epsilon^2 Pe \left( u \frac{\partial T}{\partial r} + w \frac{\partial T}{\partial z} \right) = \frac{1}{r} \frac{\partial}{\partial r} \left( r \frac{\partial T}{\partial r} + \gamma r \frac{\partial T^4}{\partial r} \right) + \epsilon^2 \frac{\partial^2}{\partial z^2} \left( T + \gamma \frac{\partial T^4}{\partial z} \right), \quad (10d)$$

where  $Pe = \rho c_p W_0 L / k_c$  is the Péclet number and  $\gamma = 4n_0^2 \sigma T^{*3} / 3\chi k_c$  (with typical values shown in table 2). The non-dimensional boundary conditions are

$$u = \frac{\partial w}{\partial r} = 0, \quad (11a)$$

on  $r = 0$ , and

$$u = w \frac{dR}{dz}, \quad (11b)$$

$$-p + 2\epsilon^2 \mu \frac{\partial u}{\partial r} = \epsilon^2 \mu \frac{dR}{dz} \left( \epsilon^2 \frac{\partial u}{\partial z} + \frac{\partial w}{\partial r} \right), \quad (11c)$$

$$\mu \left( \epsilon^2 \frac{\partial u}{\partial z} + \frac{\partial w}{\partial r} \right) = \frac{dR}{dz} \left( -p + 2\epsilon^2 \mu \frac{\partial w}{\partial z} \right), \quad (11d)$$

$$-(1 + 4\gamma T^3) \frac{\partial T}{\partial r} = \epsilon \alpha (T^4 - T_f^4) + \epsilon \beta (T - T_a), \quad (11e)$$

on  $r = R(z)$ , where  $\alpha = \sigma \epsilon_R T^{*3} L / k_c$  and  $\beta = k_h L / k_c$  (with typical values given in table 2). Finally we have

$$w(r, 0) = 1, \quad T(r, 0) = T_0, \quad w(r, 1) = w_1, \quad (12f-h)$$

where  $w_1 = W_1 / W_0$  is the ratio of axial draw speed to input speed and  $T_0 = \hat{T}_0 / T^*$  is the dimensionless inlet temperature and is given by the solution to

$$\alpha (T^4 - T_f^4) + \beta (T - T_a) = 0. \quad (13)$$

Parameter	Symbol	Approximate value
Aspect ratio	$\epsilon = R_0/L$	0.1
Reynolds number	$Re = \frac{\rho W_0 L}{\mu}$	$\lesssim 10^{-3}$
Péclet number	$Pe = \frac{\rho c_p W_0 L}{k_c}$	1400
Draw ratio	$w_1 = \frac{W_1}{W_0}$	$3 \times 10^4$
Surface radiation parameter	$\alpha = \frac{\sigma \epsilon_R T^{*3} L}{k_c}$	400
Conduction parameter	$\beta = \frac{k_h L}{k_c}$	50
Bulk radiation parameter	$\gamma = \frac{4n_0^2 \sigma T^{*3}}{3\chi k_c}$	10
furnace temperature <sup>1</sup>	$T_f(z) = \frac{\hat{T}_f}{T^*}$	$0.2 + 0.8e^{-12.5(z-0.35)^2}$
ambient temperature <sup>1</sup>	$T_a(z) = \frac{\hat{T}_a}{T^*}$	$\frac{3}{4}T_f$

Table 2: Parameter definitions (<sup>1</sup>Fillipov (2011)).

Finally, non-dimensionalizing the viscosity and taking typical values for  $a_1$  and  $b_1$  (Myers, 1989; Fillipov, 2011) gives

$$\mu(T) = \exp(22(1/T - 1)). \quad (14)$$

## 4 Fluid flow

Seeking regular parameter expansions of the form  $u = u^{(0)} + \epsilon^2 u^{(1)} + \dots$ , the flow problem, (10a-c) and (11a-c), indicates that  $w^{(0)} = w^{(0)}(z)$  and thus the flow is extensional. A similar approach to Cummings and Howell (1999),

Fitt et al. (2002) and Bohun et al. (2010) may be used to derive the following leading-order equations

$$\frac{d}{dz} \left( w^{(0)} R^{(0)2} \right) = 0, \quad (15)$$

$$\frac{d}{dz} \left( 3\bar{\mu}^{(0)} R^{(0)2} \frac{dw^{(0)}}{dz} \right) = 0, \quad (16)$$

where overbars denote the radially averaged quantity:

$$\bar{\phi}(z) = \frac{2}{R^2} \int_0^R r \phi(r, z) dr. \quad (17)$$

Equations (15) and (16) represent conservation of mass and an axial stress balance respectively. Integrating these equations and applying boundary condition (12f) yields

$$w^{(0)} R^{(0)2} = 1, \quad (18)$$

$$3\bar{\mu}^{(0)} R^{(0)2} \frac{dw^{(0)}}{dz} = F, \quad (19)$$

where  $F$  represents the (constant) tension in the fibre. In our problem we prescribe the draw speed  $w(1) = w_1$  and then  $F$  is determined as part of the solution.

## 5 Temperature

The temperature system (10d) and (11e) possesses various asymptotic limits of interest and we address these below. We note that several of the dimensional parameters given in table 1, and thus their non-dimensional counterparts given in table 2, are uncertain and may vary by up to an order of magnitude depending on the glass used, so that different limits may be appropriate in different cases.

### 5.1 Rapid heat transport across the fibre radius

#### 5.1.1 Surface radiation and conduction balance axial convection

If we suppose that  $Pe = O(1/\epsilon) = Pe^*/\epsilon$ , while all other parameters are order one, then substitution of a regular parameter expansion of the form

$T = T^{(0)} + \epsilon T^{(1)} + \dots$  into (10d) and using (11e) indicates that  $T^{(0)} = T^{(0)}(z)$  and thus radial variations in temperature are quickly smoothed out. The system is closed by proceeding to second order in (10d), integrating over the fibre radius and using (11e) and (18) to give

$$\frac{1}{2}Pe^* \frac{dT^{(0)}}{dz} = -R^{(0)} \left( \alpha \left( T^{(0)4} - T_f^4 \right) + \beta \left( T^{(0)} - T_a \right) \right). \quad (20)$$

We may substitute for  $R^{(0)}$  using (18) so that we are left to solve the system

$$3\bar{\mu}^{(0)} \frac{dw^{(0)}}{dz} = Fw^{(0)}, \quad (21a)$$

$$\frac{1}{2}\sqrt{w^{(0)}}Pe^* \frac{dT^{(0)}}{dz} = - \left( \alpha \left( T^{(0)4} - T_f^4 \right) + \beta \left( T^{(0)} - T_a \right) \right). \quad (21b)$$

In practice, the parameters  $\alpha$  and  $\beta$  may depend on fibre radius: it is thought that thinner fibres may radiate more efficiently from their surface both by Newton cooling and radiative transfer. As a result, we shall examine both the cases when  $\alpha$  and  $\beta$  are constant and when  $\alpha$  or  $\beta$  are inversely proportional to the fibre radius,  $R$ . The evolution of temperature, axial velocity and radius, with axial position for the illustrative parameter choice  $Pe^* = 1$  when we vary  $\alpha$  and  $\beta$  is depicted in figures 2 and 3 respectively. The viscosity varies through many orders of magnitude as the fibre is drawn through the furnace. The fibre temperature is heavily guided by the furnace temperature, rising to attain a peak at approximately 0.4 times the distance down the furnace, highlighting the delay compared with the furnace peak temperature (which occurs at  $z = 0.35$ ). Following this, the temperature then falls as it moves through the remainder of the furnace. The axial velocity and fibre radius both vary over a relatively small axial distance, corresponding to the region where the glass temperature is near its maximum.

We notice that the axial velocity of the glass dramatically increases as we move down the profile. Indeed, such a feature is well known in the experimental fibre drawing process. As a result it is useful to visualize the temperature profile of an element of molten glass as it moves from the preform down the furnace where it is heated and then cooled before leaving the furnace. This corresponds to determining the temperature as a function of a dimensionless ‘time variable’,  $\tau = \tau(z)$  which we identify with the time at which a given

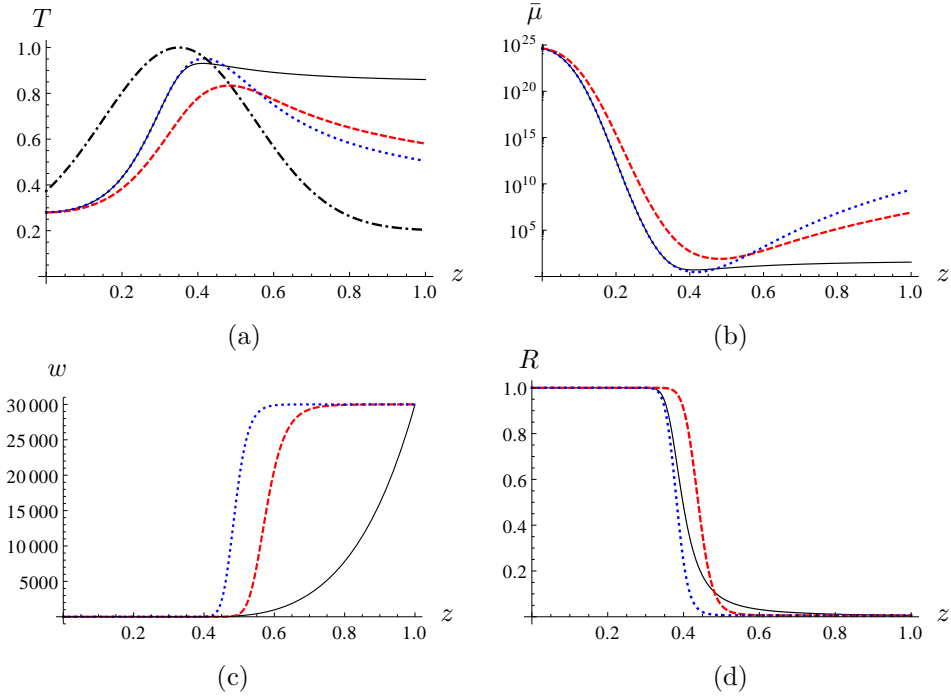


Figure 2: Influence of  $\alpha$  on the leading-order variation of (a) temperature, (b) viscosity, (c) axial velocity, and (d) radius, with axial position when  $Pe^* = 1$  and  $\beta = 1$ . The black solid line illustrates the case when  $\alpha = 1$ , and the red dashed and blue dotted lines illustrate the axial-dependent cases  $\alpha(z) = 1/R(z)$  and  $\alpha(z) = 2/R(z)$  respectively. The black dot-dashed line in (a) shows the furnace temperature  $T_f(z)$ .

glass element is at the axial position  $z$ , and is given by

$$\tau = \int_0^z \frac{1}{w(\zeta)} d\zeta. \quad (22)$$

The rapid acceleration of the glass as it moves towards the end of the furnace is clearly shown by the relation between  $\tau$  and axial position  $z$  in figure 4. Use of (22) along with the solutions  $T^{(0)}(z)$ ,  $\bar{\mu}^{(0)}(z)$ ,  $w^{(0)}(z)$  and  $R^{(0)}(z)$  provides a parametric representation of the system as a function of  $\tau$ . The rapid cooling is clearly evident in figures 5 and 6 with the temperature, viscosity, velocity and fibre radius varying dramatically in the final stages of the drawing process.

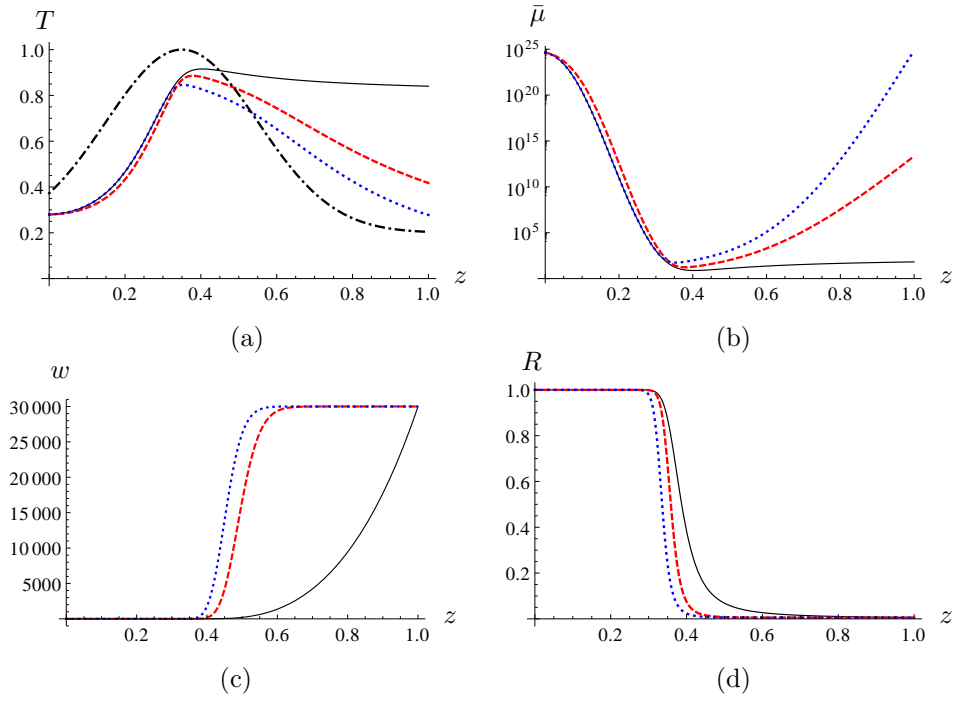


Figure 3: Effect of  $\beta$  on the leading-order variation of (a) temperature, (b) viscosity, (c) axial velocity, and (d) radius, with axial position for  $Pe^* = 1$  and  $\alpha = 1$ . The black solid line illustrates the case when  $\beta = 1$ , and the red dashed and blue dotted lines illustrate the axial-dependent cases  $\beta(z) = 1/R(z)$  and  $\beta(z) = 2/R(z)$  respectively. The black dot-dashed line in (a) shows the furnace temperature  $T_f(z)$ .

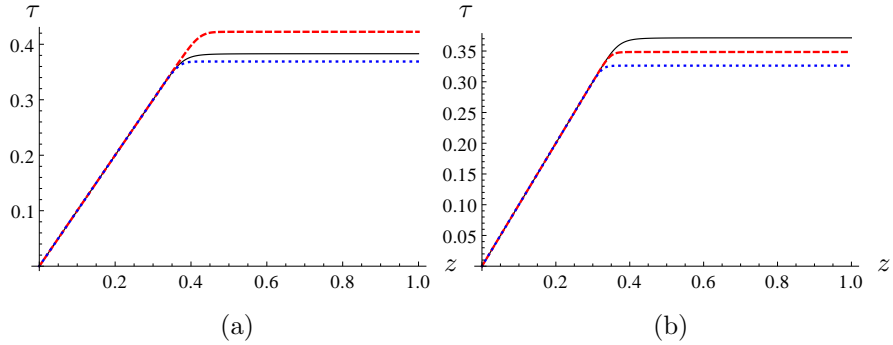


Figure 4: Time variable,  $\tau(z)$  versus axial position  $z$  given by (22) when  $Pe^* = 1$  and (a)  $\beta = 1$  and  $\alpha = 1$  (black solid line),  $\alpha(z) = 1/R(z)$  (red dashed line) and  $\alpha(z) = 2/R(z)$  (blue dotted line), and (b)  $\alpha = 1$  and  $\beta = 1$  (black solid line),  $\beta(z) = 1/R(z)$  (red dashed line) and  $\beta(z) = 2/R(z)$  (blue dotted line).

### 5.1.2 Surface radiation and conduction dominate

If we now assume that  $\alpha = O(1/\epsilon) = \alpha^*/\epsilon$  and  $\beta = O(1/\epsilon) = \beta^*/\epsilon$  then (20) implies that  $T^{(0)}(z)$  is given simply by  $\mathcal{T}(z)$ , the solution to the quartic equation

$$\alpha^* (\mathcal{T}(z)^4 - T_f(z)^4) + \beta^* (\mathcal{T}(z) - T_a(z)) = 0, \quad (23)$$

which may be expressed explicitly although, due to its complicated form, we refrain from writing it here. However, since the velocity rises towards the end of the drawing, the term neglected on the right-hand side becomes important again here and a boundary layer is thus present. Rescaling  $w^{(0)} = \mathcal{W}/\epsilon^2$  we find that the system (21) now reads

$$\frac{1}{2} \sqrt{\mathcal{W}} Pe^* \frac{dT^{(0)}}{dz} = - \left( \alpha^* (T^{(0)4} - T_f^4) + \beta^* (T^{(0)} - T_a) \right), \quad (24)$$

and we return to solving the original full system (10d). However, since the numerical simulations indicate that the velocity evolves to its final value over a fairly narrow window (near where the temperature attains its maximum) its value is approximately constant (and equal to the draw speed) for an appreciable portion of the fibre drawing. We thus propose that we may set  $\mathcal{W} = \epsilon^2 W_1 (= O(1))$ , the (known) fibre pulling speed, so that (24) provides a

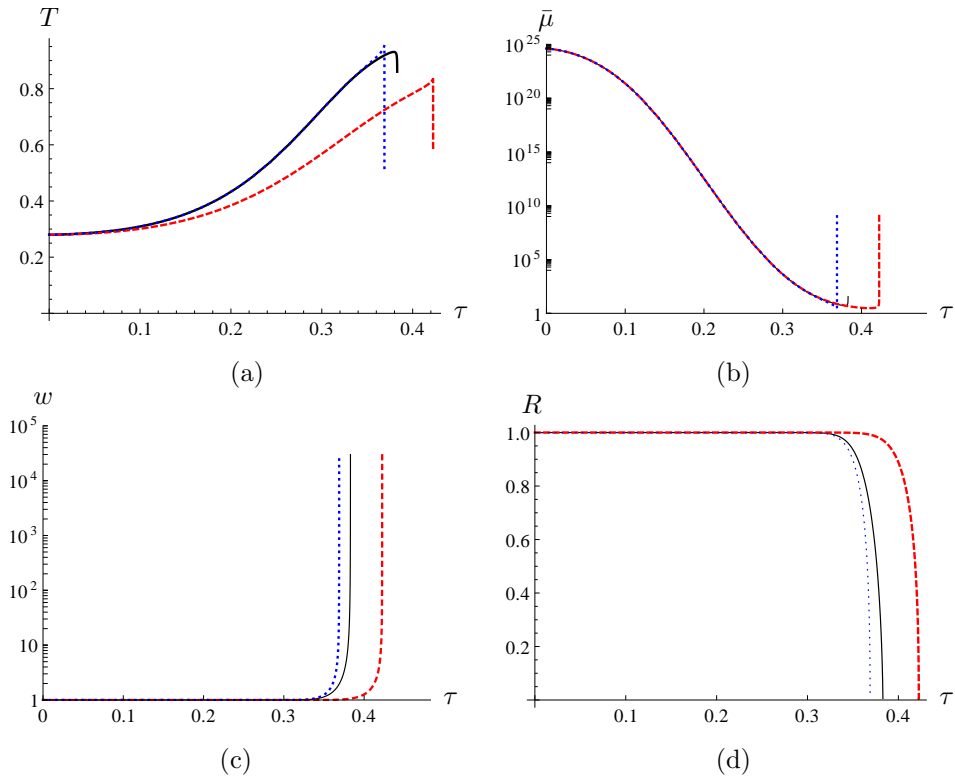


Figure 5: Leading-order variation of (a) temperature, (b) viscosity, (c) axial velocity and (d) radius with time variable  $\tau$  for  $Pe^* = 1$ ,  $\beta = 1$  and  $\alpha = 1$  (black solid line),  $\alpha(z) = 1/R(z)$  (red dashed) and  $\alpha(z) = 2/R(z)$  (blue dotted line).

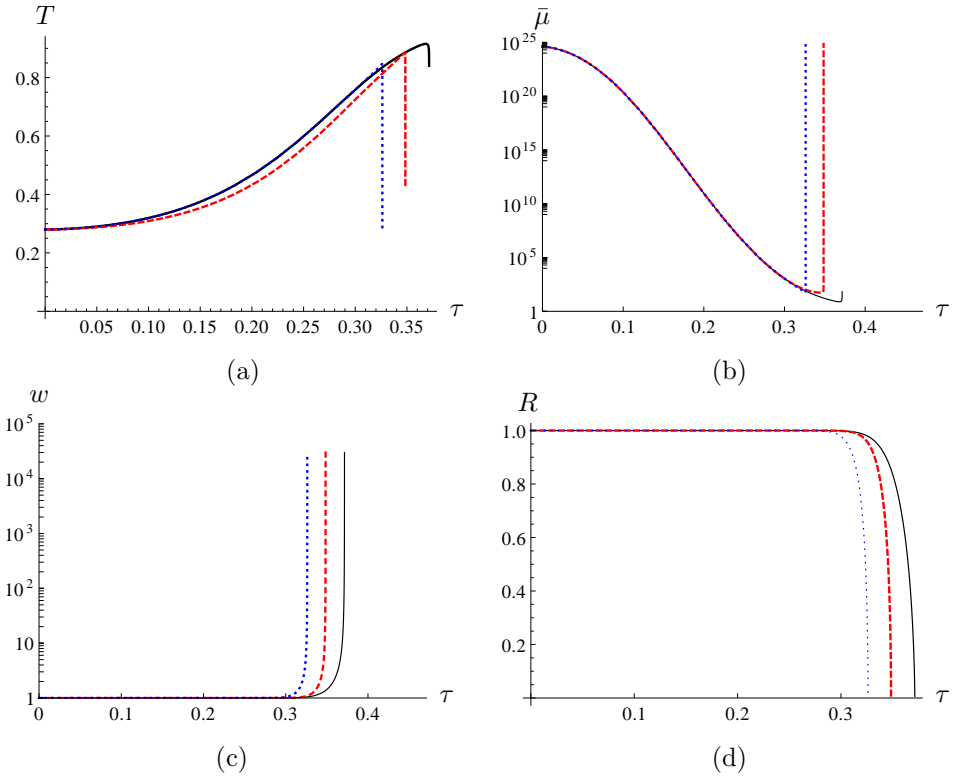


Figure 6: Leading-order variation of (a) temperature, (b) viscosity, (c) axial velocity, and (d) radius, with time variable for  $Pe^* = 1$ ,  $\alpha = 1$  and  $\beta = 1$  (black solid line),  $\beta(z) = 1/R(z)$  (red dashed) and  $\beta(z) = 2/R(z)$  (blue dotted line).

decoupled autonomous equation for  $T^{(0)}$  in this region which may be solved implicitly to give

$$z(T^{(0)}) = \int_1^T -\frac{Pe^* ds}{R(\alpha^*(s^4 - T_f^4) + \beta^*(s - T_a))}. \quad (25)$$

By approximating the temperature by the solution to (23) until  $T^{(0)}$  reaches its maximum value, where the solution is patched to (25) this provides an approximation to the full temperature distribution. Once determined, (21a) provides an ODE for just  $w^{(0)}$ , and  $R^{(0)}$  is then determined by (18). In figure 7 we compare the asymptotic solutions given here to the solution to the full coupled system (21). The agreement is excellent, with the full numerical solution and asymptotic approximation almost indistinguishable. The asymptotic solutions derived here thus provide a simple yet accurate description of the system behaviour. Plots of evolution as a function of the time variable  $\tau$  are also displayed in figure 8.

### 5.1.3 First-order correction

Since the leading-order system depends only on axial position, to quantify the radial variations we must analyse the system at the next order. In doing so, provided  $w^{(0)}$  is of order unity, which we have seen is true up to the point at which the glass reaches its maximum temperature, equation (11e) indicates that

$$T(r, z) = T(z) + \epsilon \left[ \frac{Pe^*(r^2 - R^{(0)2})w^{(0)}T'(z)}{4(1 + 4\gamma T^3)} + T^{(1)}|_{r=R(z)} \right], \quad (26)$$

where the final term depends on the size of  $\alpha$  and  $\beta$ . In the case considered above, that is  $\alpha = \alpha^*/\epsilon$ ,  $\beta = \beta^*/\epsilon$ , we find from (11e) that

$$T^{(1)}|_{r=R(z)} = -\frac{Pe^*w^{(0)}T'(z)R}{2(\beta^* + 4\alpha^*T(z)^3)}. \quad (27)$$

However, we may also consider asymptotically larger values of  $\alpha$  and  $\beta$ , for which we find the following formulae:

$$T^{(1)}|_{r=R(z)} = \begin{cases} -\frac{\beta^*(T_f - T_a)}{\hat{\alpha} 4T_f^3}, & \alpha = \hat{\alpha}/\epsilon^2, \beta = \beta^*/\epsilon, \\ \frac{\alpha^*}{\hat{\beta} (T_a^4 - T_f^4)}, & \alpha = \alpha^*/\epsilon, \beta = \hat{\beta}/\epsilon^2, \\ 0, & \alpha = \hat{\alpha}/\epsilon^2, \beta = \hat{\beta}/\epsilon^2, \end{cases} \quad (28)$$

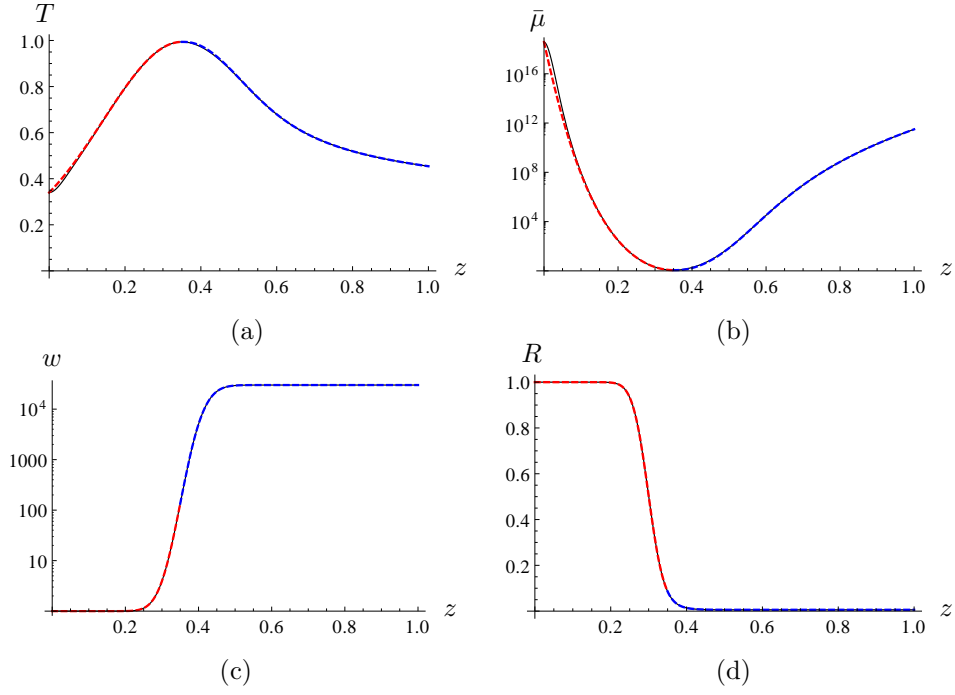


Figure 7: (a) Variation of leading-order temperature with axial position given by (20) when  $Pe = 1$ ,  $\epsilon\alpha = \alpha^* = 50$  and  $\epsilon\beta = \beta^* = 5$  (black). The red dashed line shows the asymptotic solution  $\mathcal{T}$  given by (23) and the blue dashed line shows the asymptotic solution given by (25); figures (b), (c) and (d) show respectively the viscosity, axial velocity and radius and the corresponding asymptotic solutions.

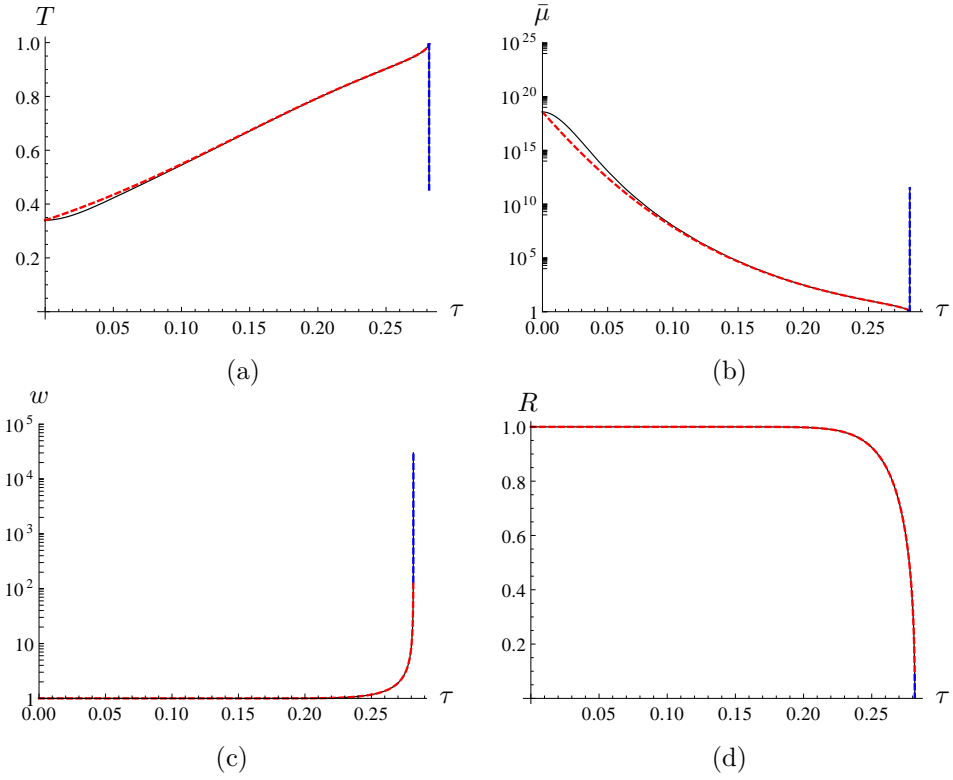


Figure 8: (a) Variation of leading-order temperature with  $\tau$ , given by (20) when  $Pe = 1$ ,  $\epsilon\alpha = \alpha^* = 50$  and  $\epsilon\beta = \beta^* = 5$  (black). The red dashed line shows the asymptotic solution  $\mathcal{T}$  given by (23) and the blue dashed line shows the asymptotic solution given by (25); figures (b), (c) and (d) show respectively the viscosity, axial velocity and radius and the corresponding asymptotic solutions.

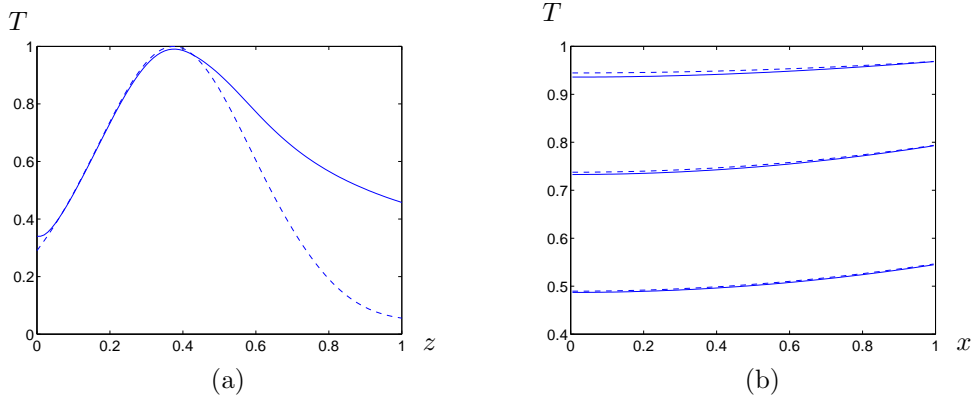


Figure 9: Numerical (solid) and asymptotic (dashed) results for the temperature against (a) axial position, with  $x = 0$ , and (b) scaled radial position,  $x$ , with  $z = \{0.1, 0.2, 0.3\}$ , taking  $\epsilon = 0.1$ ,  $Pe^* = 1$ ,  $\hat{\alpha} = \hat{\beta} = 5$ ,  $\gamma = 0$ .

where  $\hat{\alpha}$ ,  $\hat{\beta}$  are of order unity.

We plot the temperature profile (26) against both axial position and scaled radial position,  $x(r, z) = r/R^{(0)}(z)$ , for the case  $\alpha = \hat{\alpha}/\epsilon^2$ ,  $\beta = \hat{\beta}/\epsilon^2$  in figure 9, showing excellent agreement with the numerical solution to the full two-dimensional problem (see §5.2), at least until the temperature reaches its maximum. After this point the axial velocity  $w^{(0)}$  increases rapidly and we can no longer ignore the left-hand side of (10d). We also note that there is an initial transient in which (26) diverges from the numerical solution, but this is just a consequence of imposing a uniform temperature profile at  $z = 0$  in the full problem.

## 5.2 Transport across the fibre balancing convection

### 5.2.1 Surface radiation and conduction balance convection

When  $Pe = O(1/\epsilon^2) = \mathcal{P}/\epsilon^2$ , heat transfer across the fibre is balanced by the convective transport. In this case the convective terms on the left-hand side of (10d) appear at leading order and  $T^{(0)}$  depends on both  $r$  and  $z$ . However, by changing variables into a coordinate frame that adapts to the radius of the fibre, via

$$x(r, z) = \frac{r}{R^{(0)}(z)}, \quad \zeta = \mathcal{P} z, \quad (29)$$

transforms the system (10*d*) and (11*e*) into

$$\frac{\partial T^{(0)}}{\partial \zeta} = \frac{1}{x} \frac{\partial}{\partial x} \left( x \frac{\partial T^{(0)}}{\partial x} (1 + 4\gamma T^{(0)3}) \right), \quad (30a)$$

with

$$-\frac{\partial T^{(0)}}{\partial x} (1 + 4\gamma T^{(0)3}) = \alpha^* R^{(0)} (T^{(0)4} - T_f^4) + \beta^* R^{(0)} (T^{(0)} - T_a), \quad (30b)$$

on  $x = 1$ , where we have set  $\alpha = \alpha^*/\epsilon$  and  $\beta = \beta^*/\epsilon$  as before, as this provides the richest limit in which surface radiation and conduction balance convection.

In general, we must solve (30*a*) numerically together with (18)–(19). We discretize the differential equations using second-order centred differences for the spatial derivatives, and integrate in time using the MATLAB differential-algebraic equation solver `ode15s`, treating (19) as an algebraic constraint at each time-step. Once the solution is found, given an initial guess for  $F$ , the process is repeated iteratively until boundary condition (12*h*) is satisfied at the end of the domain.

### 5.2.2 Industrially relevant regime

Based on the parameter values given in table 1, we take  $\mathcal{P} = 1$ ,  $\alpha^* = 50$ ,  $\beta^* = 5$ ,  $\gamma = 10$ , and present numerical results for the temperature and free-surface profiles in figure 10. As expected, we see that the temperature now varies across the radius of the fibre, being hottest at the edge and coolest in the middle.

Although we are able to solve the full numerical system numerically, we note that in the limit of strong radiation (as suggested by our parameter values) and/or strong cooling, equations (30*a*)–(30*b*) de-couple leading to a simplified system. For example, setting  $\alpha = \hat{\alpha}/\epsilon^2$  and  $\beta = \hat{\beta}/\epsilon^2$  where  $\hat{\alpha}$  and  $\hat{\beta}$  are  $O(1)$ , the leading-order boundary condition (30*b*) simplifies to  $T^{(0)} = \mathcal{T}(\zeta)$  on  $x = 1$  where  $\mathcal{T}$  is again given by (23) with  $\alpha^*$ ,  $\beta^*$  replaced by  $\hat{\alpha}$ ,  $\hat{\beta}$  respectively.

### 5.2.3 The effect of bulk radiation

We now consider the role of bulk radiation, which for  $Pe = O(1/\epsilon^2)$  comes in at leading order when  $\gamma = O(1)$ , as assumed thus far. From (30*a*)–(30*b*)

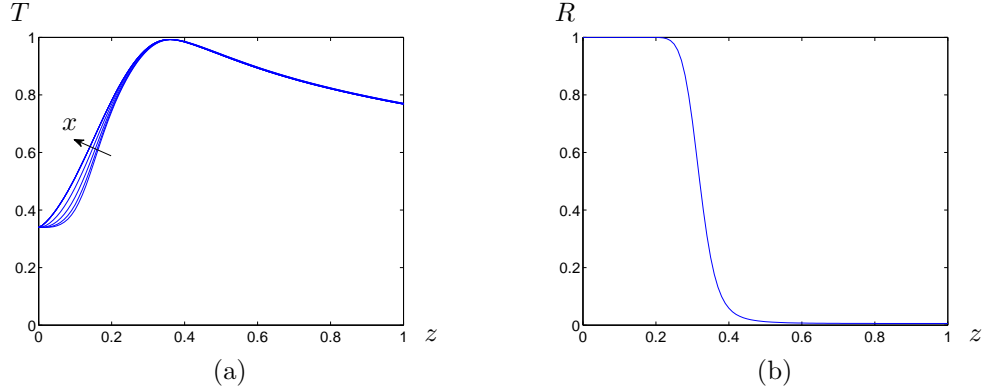


Figure 10: (a) Variation in leading-order temperature with axial position for radial coordinate  $x = \{0, 0.2, 0.4, 0.6, 0.8, 1\}$  in the case  $\mathcal{P} = 1$ ,  $\alpha^* = 50$ ,  $\beta^* = 5$ ,  $\gamma = 10$ . Figure (b) shows the corresponding fibre radius.

we see that if  $\gamma \gg 1$ , bulk radiation dominates so that the temperature is approximately constant across the fibre. On the other hand, if we now set  $\gamma = 0$ , that is, zero bulk radiation, the model reduces to

$$\frac{\partial T^{(0)}}{\partial \zeta} = \frac{1}{x} \frac{\partial}{\partial x} \left( x \frac{\partial T^{(0)}}{\partial x} \right) \quad \text{in } 0 < x < 1, \quad (31a)$$

$$T^{(0)} = \mathcal{T}(\zeta) \quad \text{at } x = 1, \quad (31b)$$

$$T^{(0)} \text{ bounded} \quad \text{at } x = 0, \quad (31c)$$

$$T^{(0)} = \mathcal{T}(0) \quad \text{at } \zeta = 0, \quad (31d)$$

and in this case we are able to solve explicitly for the temperature. We let  $T^{(0)}(x, \zeta) = \mathcal{T}(\zeta) + \hat{T}(x, \zeta)$  and pose the ansatz that

$$\hat{T}(x, \zeta) = \sum_{m=1}^{\infty} f_m(\zeta) J_0(\lambda_m x), \quad (32)$$

where  $J_0$  is the lowest-order Bessel function and  $\lambda_m$  are the roots of  $J_0$ . We find that  $f_m$  satisfies

$$f'_m + \lambda_m^2 f_m = -\frac{2\mathcal{T}'}{\lambda_m J_1(\lambda_m)}, \quad (33)$$

where  $J_1$  is the first-order Bessel function and the solution for  $f_m$  is given by

$$f_m = -\frac{2e^{-\lambda_m^2\zeta}}{\lambda_m J_1(\lambda_m)} \int_0^\zeta \mathcal{T}'(s) e^{-\lambda_m^2 s} ds, \quad (34)$$

and so the solution for  $T^{(0)}$  is

$$T^{(0)}(x, \zeta) = \mathcal{T}(\zeta) + \sum_{m=1}^{\infty} -\frac{2J_0(\lambda_m x) e^{-\lambda_m^2 \zeta}}{\lambda_m J_1(\lambda_m)} \int_0^\zeta \mathcal{T}'(s) e^{-\lambda_m^2 s} ds. \quad (35)$$

We plot (35) including ten terms in the summation in figure 11(a) showing very good agreement with numerical results everywhere except near the origin, where the modulus of the terms in the expansion start becoming very large leading to numerical errors. Once we have found the temperature, we may now calculate  $\bar{\mu}$  and solve (18)–(19) iteratively to find  $w$ ,  $R$ , and  $F$ . The corresponding fibre radius is shown in figure 11(b). In addition to giving a simple explicit solution, (35) also provides a validation for the full two-dimensional numerics.

We compare our solution for zero bulk radiation to one with non-zero bulk radiation, but all other parameters kept constant, in figure 11(c)–(d). As expected, with zero bulk radiation we find a greater variation in temperature across the fibre, which leads to a greater radially averaged glass viscosity so that a greater force is required to pull the fibre through the furnace. Increasing  $\gamma$  aids the heat transfer through the filament cross-section and hence smooths the temperature profile out.

## 6 Discussion

In this report we have derived and analysed an extensional flow model to describe the evolution of an axially evolving optical fibre, in which we track the radius of the fibre, the speed of the fibre and the temperature. We incorporated energy transfer due to conduction, convection, bulk and surface radiation, and through convective cooling from the air, assuming that the fibre is optically thick. We also included the dependence of the viscosity on temperature.

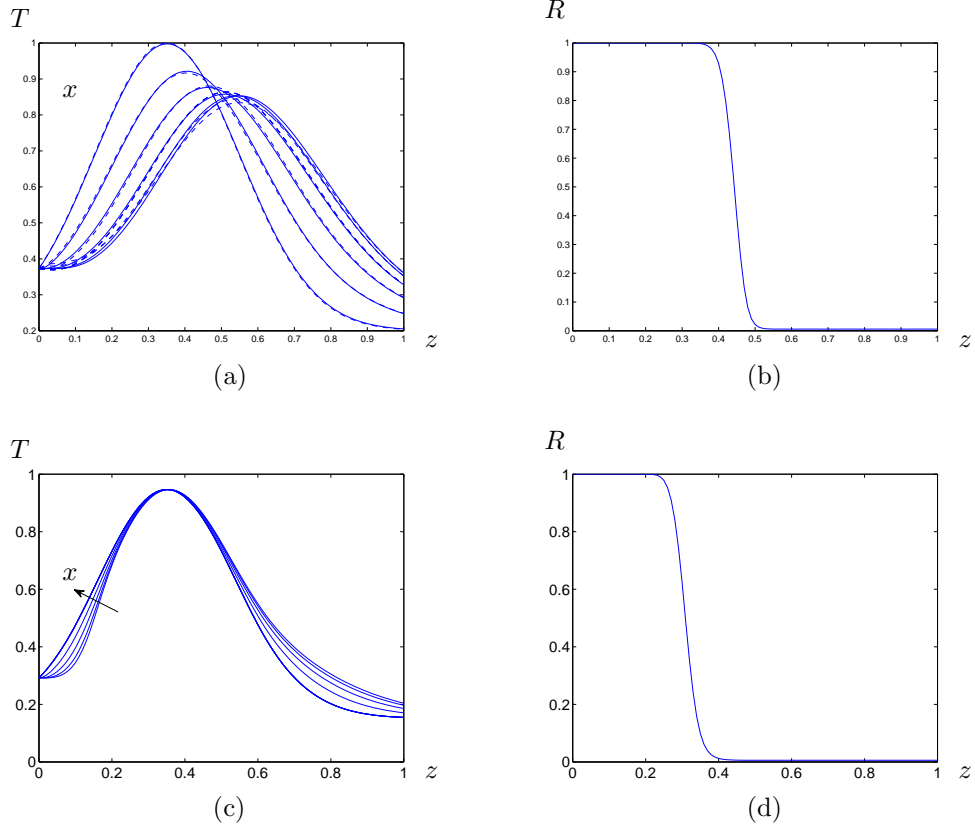


Figure 11: (a) Variation in leading-order temperature with axial position for  $x = \{0, 0.2, 0.4, 0.6, 0.8, 1\}$  in the case  $Pe^* = 1$ ,  $\hat{\alpha} = \hat{\beta} = 1$ ,  $\gamma = 0$ . The solid lines correspond the numerical solution of (31a) while the dashed lines correspond to the exact solution (35) taking ten terms in the expansion. The corresponding fibre radius is shown in (b). Figures (c)–(d) are the same as (a)–(b) except  $\gamma = 10$ .

The model was first solved numerically in the limit where the temperature didn't vary across the fibre. Using a change of variables, the solutions were presented in evolving in "time" and exhibited a boundary layer near the end of the evolution. The structure of this solution was determined in the original coordinate system using asymptotic analysis. The domain decomposed into an initial region where the temperature is set by a balance between surface radiation and convective cooling, in which the velocity and fibre radius vary significantly, and then a later region where the radius and velocity are effectively constant and the evolution of the temperature also involves bulk convection.

Other interesting parameter limits of the model were explored using asymptotics and numerics. In the industrially relevant limit, the temperature varies along and across the fibre, but the qualitative features are the same as in the radially invariant case. The model can be used to assess the relative importance of surface cooling, surface radiation, bulk radiation and standard heat transfer on the evolution of the fibre. In particular, including bulk radiation smooths over the temperature profile across the fibre, as shown in figure 11.

There are two key things to do to extend the model. As discussed in §2.1, firstly, we should consider the case when the fibre is optically thin. In this case, determining the energy transfer would involve tracing rays within the fibre, see Liu and Rogg (1996) which describes the procedure for looking at radiative transfer in a flame. Secondly, we should solve for the temperature field outside the fibre, taking into account that the convective transfer to the fibre will be affected by the speed of the fibre and that the presence of the air will affect the (external) radiative transfer.

## References

- Bohun, C. S., Breward, C. J. W., Cummings, L. J., and Witelski, T. P. (2010). Two problems on the flow of viscous sheets of molten glass. *Proc. 26<sup>th</sup> Annual Workshop on Mathematical Problems in Industry*.
- Carslaw, H. and Jaeger, J. (1959). *Conduction of heat in solids*. Oxford: Clarendon Press, 1959, 2nd ed., 1.
- Choudhury, S. R., Jaluria, Y., and Lee, S. H.-K. (1999). A computational

- method for generating the free-surface neck-down profile for glass flow in optical fiber drawing. *Numer. Heat Transfer Part A*, 35:1–24.
- Cummings, L. J. and Howell, P. D. (1999). On the evolution of non-axisymmetric viscous fibres with surface tension, inertia and gravity. *J. Fluid Mech.*, 389(1):361–389.
- Fillipov, A. (2011). Private communication.
- Fitt, A., Furusawa, K., Monro, T., Please, C., and Richardson, D. (2002). The mathematical modelling of capillary drawing for holey fibre manufacture. *J. Eng. Math.*, 43(2):201–227.
- Huang, H., Miura, R., and Wylie, J. (2008). Optical fiber drawing and dopant transport. *SIAM J. Appl. Math.*, 69(2):330–347.
- Huang, H., Miura, R. M., Ireland, W. P., and Puil, E. (2003). Heat-induced stretching of a glass tube under tension: Application to glass microelectrodes. *SIAM J. Appl. Math.*, 63:1499–1519.
- Liu, Y. and Rogg, B. (1996). Prediction of radiative heat transfer in laminar flames. *Combust. Sci. Tech.*, 118:127–145.
- Myers, M. (1989). A model for unsteady analysis of preform drawing. *AIChE J.*, 35(4):592–602.
- National Institute of Standards & Technology (1991). *Standard Reference Material 710a. Soda-Lime-Silica Glass*. <http://glassproperties.com/standards>.
- Paek, U. and Runk, R. (1978). Physical behavior of the neck-down region during furnace drawing of silica fibers. *J. Appl. Phys.*, 49(8):4417–4422.
- Šarboh, S. D., Milinković, S. A., and Debeljković, D. L. J. (1998). Mathematical model of the glass capillary tube drawing process. *Glass Technol.*, 39:53–67.